Electric polarization reversal and nonlinear magnetoelectric coupling in the honeycomb antiferromagnet $Fe_4Nb_2O_9$ single crystal

J. H. Zhang,[1] Y. S. Tang,[1] L. Lin,[1,2,*] L. Y. Li,[3] G. Z. Zhou,[1] B. Yang,[1] L. Huang,[1] X. Y. Li,[1] G. Y. Li,[1] S. H. Zheng,[4] M. F. Liu,[4] M. Zeng,[3] D. Wu,[1] Z. B. Yan,[1] X. K. Huang,[5] C. Chen,[5] X. P. Jiang,[5] and J.-M. Liu[1]

[1]*Laboratory of Solid State Microstructures, Nanjing University, Nanjing 210093, China*

[2]*Department of Applied Physics, College of Science, Nanjing Forestry University, Nanjing 210037, China*

[3]*Institute for Advanced Materials, Guangdong Provincial Key Laboratory of Optical, Information Materials and Technology, South China Academy of Advanced Optoelectronics, South China Normal University, Guangzhou 510006, China*

[4]*Institute for Advanced Materials, Hubei Normal University, Huangshi 435002, China*

[5]*School of Materials Science and Engineering, Jingdezhen Ceramic Institute, Jingdezhen 333001, China*

(Received 18 February 2022; revised 21 August 2022; accepted 10 January 2023; published 27 January 2023)

As a new magnetoelectric material, honeycomb-based antiferromagnet $Fe_4Nb_2O_9$ has attracted a great deal of attention due to its prominent magnetoelectric (ME) coupling and high Néel temperature, while the physics of magnetoelectricity is far from understood. In the present study, we present our systematic investigations of the anisotropic ME effect, electric polarization reversal, and nonlinear ME effect of $Fe_4Nb_2O_9$ single crystals, thus highlighting the phase diagram extended down to 10 K. Our results provide clear evidence for electric polarization reversal driven by magnetic field (H) along the [110] and [1-10] directions, respectively, while no such polarization reversal occurs as H is applied along the [001] direction. The nonlinear ME effects and electric control of magnetism are unambiguously demonstrated. In addition, the angular-dependent probing reveals a 2θ rotation of the induced electric polarization around the c axis upon the rotation of magnetic field by an angle θ. The electric polarization responses and concomitant ME coupling are well explained by means of the metal-ligand hybridization p-d mechanism. This work represents an essential step forward in the understanding of ME coupling not only in this $A_4M_2O_9$ honeycomb magnet.

DOI: 10.1103/PhysRevB.107.024108

I. INTRODUCTION

Multiferroics, which are materials that have more than one primary ferroic order in the single phase, have brought out plenty of exotic physical phenomena [1–7]. Among them, the linear magnetoelectric (ME) effect, in which the induced electric polarization (P) or magnetization (M) is proportional to the applied magnetic field (H) or electric field (E), has drawn a great deal of interest due to the potential applications in novel devices [8–10]. The simultaneous breaking of spatial inversion and time-reversal symmetry is the key to allow the ME effect. These compounds usually crystallize in centrosymmetric structures with collinear antiferromagnetic (AFM) order, where a perfect match between magnetic and lattice structures is required [11], as exemplified by Cr_2O_3 [12], $LiCoPO_4$ [13], Sm_2BaCuO_5 [14], and $PbCu_3TeO_7$ [15]. However, nonlinear ME behavior can be induced by diverse magnetic orders in magnets with noncentrosymmetric crystal lattices, such as $Fe_2Mo_3O_8$ [16,17], Cu_2OSeO_3 [18], and $GdFeO_3$ [19], among many others.

Recently, the corundum-type compound $Fe_4Nb_2O_9$ was reported to exhibit significant ME effect below its Néel temperature $T_N \sim 90$ K, accompanied by two broad dielectric features at T_N and 77 K in polycrystalline state [20]. It crystallizes in a trigonal space group P-3c1 with two distinct crystallographic Fe sites (Fe1 and Fe2), as schematically shown in Fig. 1(a). By using the neutron powder diffraction, Jana *et al.* determined the magnetic moments at the Fe1 and Fe2 sites arranged antiferromagnetically in the ab plane and assigned it either $C2/c'$ or $C2'/c$ magnetic symmetry [21]. The adjacent Fe1 and Fe2 layers were ferromagnetically coupled along the c axis. In addition, a structure transition from trigonal P-3c1 to monoclinic $C2/c$ occurred around $T_{str} \sim 77$ K (70 K, 85 K), which was not identified in other $A_4M_2O_9$ (A = Mn, Co, M = Nb, Ta) members [22–27]. It was later shown in Ref. [28] that $Fe_4Nb_2O_9$ has the magnetic space group $C2/c'$ (magnetic point group $2/m'$), described as antiferromagnetically coupled ferromagnetic chains along the c axis with all spins confined in the ab plane and a small canting angle of 5.81° between the adjacent Fe1-Fe2 layers. Figures 1(b)–1(e) show the detailed magnetic structures of Fe1 and Fe2 layers in the trigonal P-3c1 and monoclinic $C2/c$ phases, respectively. Indeed, imposed by this magnetic symmetry, the ME coupling tensor has in principle *five* nonzero terms, which were confirmed by magnetodielectric measurements [28]. However, recently Zhang *et al.* reported the existence of *nine* nonzero components in linear ME tensor α_{ij} reflected by H-induced electric polarization above 90 K, demonstrating a much lower magnetic point group of $-1'$ that should govern the canted antiferromagnetic structure [29].

*Corresponding author: llin@njfu.edu.cn

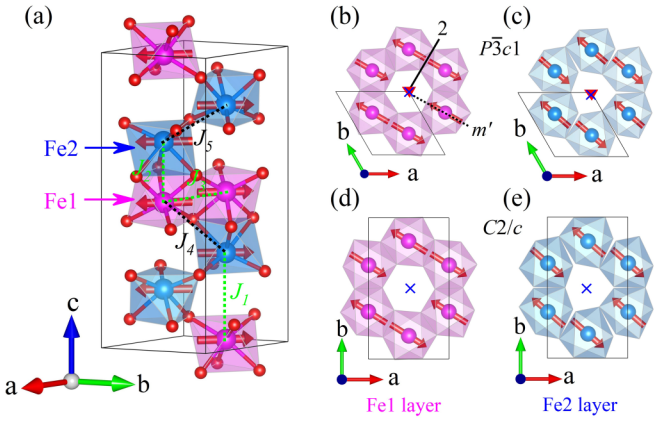

FIG.1. (a) Schematic illustration of crystal structure of P-3c1 phase in $Fe_4Nb_2O_9$. Green and black dashed lines denote the ferromagnetic and antiferromagnetic exchange interactions. Top view of magnetic structures of Fe1 layer and Fe2 layer in (b), (c) P-3c1 phase and (d), (e) $C2/c$ phase, respectively. Red arrows denote the magnetic moments of Fe^{2+} ions. The symbol of "×" denotes the space inversion center, and red triangle presents the threefold symmetry along the c axis. Solid black line in (b) denotes the twofold rotation symmetry and the dashed black line denotes the mirror symmetry.

Given the aforementioned incompatible results, one is highly concerned with the alignment of electric polarization, as seen along different crystallographic directions down to low temperature (T), while unfortunately so far all the ME characterizations of $Fe_4Nb_2O_9$ single crystal were carried out on high-T trigonal P-3c1 phase, noting that pyroelectric current method at high temperature should be more cautiously employed due to possible consequence of thermal activation. In fact, Maignan *et al.* reported the ME coupling and sign change of pyroelectric current at low T in polycrystalline sample [20]. In addition, the response of electric polarization against H shows opposite behavior for $T \sim 10$ K and $T \sim 77$ K, indicating more complex ME coupling than that observed in $Co_4Nb_2O_9$ and $Mn_4Nb_2O_9$ [22,25]. An important question is how the electric polarization evolves upon decreasing T. In order to clarify these issues, it is thus urgently needed to revisit this compound by uncovering the intrinsic ME response.

In this work, we unveil the anisotropic ME coupling and electric polarization reversal by a series of characterizations of magnetic susceptibility, specific heat, and ME response of $Fe_4Nb_2O_9$ single crystals. We observe unusual electric polarization reversal driven by H applied, respectively, along the [110] and [1-10] directions. In particular, nonlinear ME effect associated with the spin rotation and magnetic domain realignment can be driven by magnetic field beyond the threshold field H_c for magnetization, in stark contrast to the linear ME response only for $Co_4Nb_2O_9$ although it shares the magnetic and lattice structures identical to $Fe_4Nb_2O_9$. In the low-H region, a linear ME coefficient up to -91.5 ps/m, one of the largest values in this family, is obtained. The phase diagrams for H, respectively aligned along the [110] and [001] directions, have been constructed, showing the strong anisotropy of ME effect. It is suggested that our experimental observations can be well explained based on the p-d hybridization mechanism, thereby revealing the rich emergent ME phenomena that deserve further exploration.

II. EXPERIMENTAL DETAILS

A. Synthesis of single crystals

First, the $Fe_4Nb_2O_9$ powder was prepared by the conventional solid-state reaction. Stoichiometric amounts of high-purity Fe_2O_3, Nb_2O_5, and Nb were sintered in an evacuated quartz tube at 1100 ° C for 24 h. The obtained powder was reground and compressed into a uniform rod under hydrostatic pressure of 70 MPa, then sintered in an evacuated quartz tube at 1100 °C for 10 h. Subsequently, the well-sintered polycrystalline bars were used as precursors for single-crystal growth.

The single crystals were grown by optical floating furnace (Cyberstar, MF-2400) with the feed and seed growth speed of 5 mm/h in a high-purity Ar gas flow. A cylindrically shaped single crystal 6 mm in diameter and 10 cm in length of black shining surface was obtained. The crystallinity of as-grown crystals was characterized by x-ray powder diffraction (D8 ADVANCE, Bruker) with Cu K_α source (wavelength $\lambda = 1.5406$ Å). Crystallographic orientation was determined using the back-reflection Laue detector (MWL120, Multiwire Laboratories, Ltd.) and the Rietveld structural refinement was performed by GSAS program [30]. The crystal structure was visualized by VESTA software [31].

B. Multiferroic characterizations

The dc magnetic susceptibility (χ) as a function of T was measured using the Quantum Design superconducting quantum interference device magnetometer under the zero-field cooled (ZFC) and field-cooled (FC) modes with the cooling field of 1.0 kOe. The H-dependent magnetization (M) was measured using the vibrating sample magnetometer in the Physical Property Measurement System (PPMS, Quantum Design). The specific heat (C_p) was measured by PPMS in a standard procedure in the temperature range of 5 to 140 K.

For the anisotropic ME characterizations, well-aligned crystals with the largest surfaces, respectively normal to the [110], [1-10], and [001] directions, were required, and they were cut into plates for the electric measurements. Here, we measured different electric currents (I) from which electric polarization P is evaluated:

(i) Pyroelectric current (I_T) which was probed as a function of T from the lowest T ($\sim$10 K) in the pyroelectric current mode, under zero or nonzero H. The electric polarization P was then obtained by integrating the $I_T(T)$ data, as done for the standard pyroelectric measurement.

(ii) ME current (I_H) which was probed as a function of H in the H-cycling mode at the isothermal condition (fixed T). It should be mentioned that no absolute electric polarization can be obtained from this dataset of current, and the obtained polarization signals are the change in electrical polarization, ΔP_H, induced by magnetic field H. Therefore, the integration of the I_H data in the H cycle produces this change at fixed T.

In practical measurements, both currents I_T and I_H were collected only after the samples experienced the ME annealing procedure, carefully carried out in order to reduce the influence of leakage current or other sources. In de-

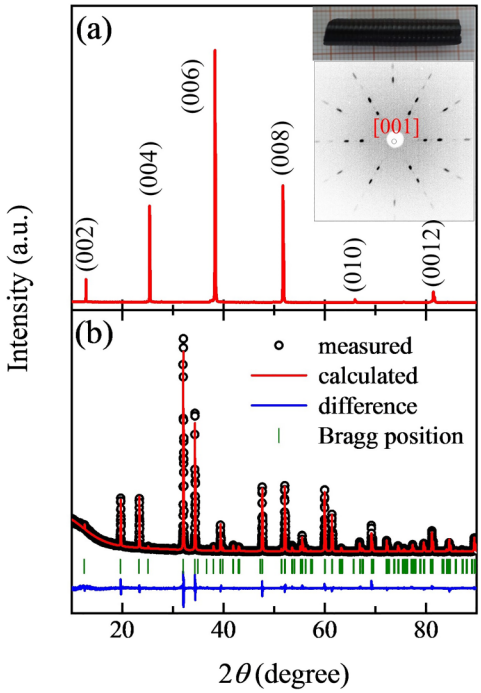

FIG. 2. (a). XRD pattern of as-grown single crystal at room temperature. The inset shows the photograph of the single crystal and the Laue diffraction spots obtained along the [001] direction. (b) XRD diffraction pattern and the Rietveld refinement of the crushed single crystal measured at room temperature.

tail, the sample was initially poled with $-H = -9\,\mathrm{T}$, $+E = +6.67\,\mathrm{kV/cm}$ from $T = 120$ to 80 K, below which a small $E = +0.1\,\mathrm{kV/cm}$ was applied until $T = 10\,\mathrm{K}$. The short-circuited procedure for sufficient time (30 min) was performed before each measurement to avoid the influence of the injected charges. When the background of electrical current was less than 0.05 pA, the pyroelectric current I_T was collected by sweeping T from 10 to 120 K on warming at a rate of 3 K/min under selected H values. The ME current I_H and H-induced polarization (ΔP_H) were measured under selected T upon H ramping from $-H \rightarrow +H \rightarrow -H$ at a rate of 100 Oe/s using the same ME poling procedure.

III. RESULTS

Before presenting the magnetic data, the quality of single crystals was carefully checked at room temperature as shown in Fig. 2(a). The inset of Fig. 2(a) shows the picture of one segment of the as-grown crystal. The c plane is carefully oriented and cut with the aid of Laue and x-ray diffractions (XRD), and the perfect diffraction spots and peaks from the [00l] direction demonstrate the high quality of the crystal. In Fig. 2(b), the XRD pattern is presented, with slow-scan pattern and Rietveld refinement of the crushed single crystal at room temperature. All the diffraction peaks are well indexed by trigonal space group P-3c1. The refined unit-cell parameters $a = b = 5.2311$ Å, and $c = 14.2242$ Å, with reliability parameters $R_{wp} = 8.84\%$ and $\chi^2 = 2.49\%$, consistent with previous report [20].

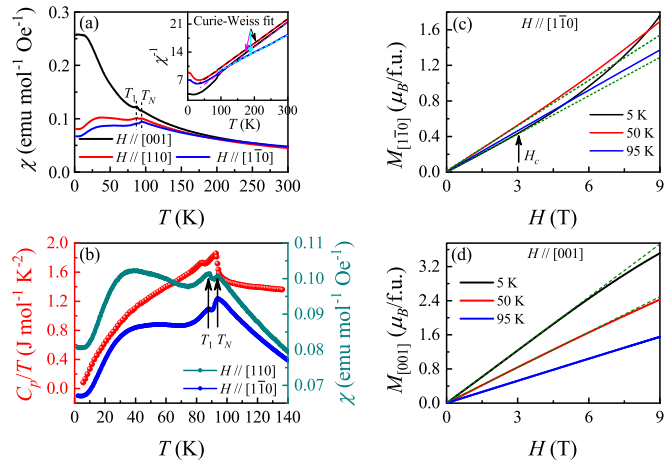

FIG. 3. (a) Magnetic susceptibility $\chi(T)$ curves measured under ZFC mode with magnetic field $H = 0.1$ T applied along the [001], [110], and [1-10] directions. The inset shows the Curie-Weiss fitting in the paramagnetic region. (b) T-dependent C_p/T, $\chi_{[1\text{-}10]}$, and $\chi_{[110]}$ curves. (c) H-dependent magnetization (M) measured at different T under the magnetic field along [1-10] and (d) [001] directions. Green dashed lines in (c) and (d) as guide to the eye indicate the linear relationship.

A. Magnetic anomalies and specific heat

Figure 3(a) displays the measured dc magnetic susceptibility $\chi(T)$ curves under the ZFC mode with measuring $H = 0.1\,\mathrm{T}$ applied, respectively, along the [001], [110], and [1-10] directions. While the normal $\chi(T)$ dependence from the high-T side is shown, the first anomaly in small kink feature appears at Néel temperature $T_N = 93\,\mathrm{K}$ and is assigned as the long-range AFM ordering. The reported values of T_N are somehow author dependent, e.g., $T_N \sim 90\,\mathrm{K}$ [20] and $= 97\,\mathrm{K}$ [28], as evaluated from polycrystalline samples and single crystals, respectively. Here, the remarkable $\chi(T)$ difference along the [001] and [110] directions indicates the magnetic moments mainly constrained in the ab plane [28]. By analyzing the $\chi(T)$ data above $T = 100\,\mathrm{K}$, one sees that the Curie-Weiss temperature (θ_{cw}), as extracted from the data along the [001], [110], and [1-10] directions, are -52.57, -71, and -126.5 K, respectively.

More interestingly, another evident anomaly which has not been observed in previous works shows up at $T = T_1 \sim 87\,\mathrm{K}$, as seen in Fig. 3(a). To further investigate this emergent anomaly, we measured the specific heat (C_p/T) under zero field, as shown in Fig. 3(b), where the $\chi(T)$ data with measuring field H//[110] and H//[1-10] are plotted as well for reference. In addition to the featured λ-shape peak located at T_N, an additional anomaly does emerge at T_1, in accordance with the anomaly in the $\chi(T)$ curves at T_1.

In principle, there are five nearest-neighbor and next-nearest neighbor exchanges, i.e., ferromagnetic exchanges J_1 (strong), J_2, J_3, and strong AFM exchanges J_4 and J_5, as illustrated in Fig. 1(a). Because J_2 and J_3 are relatively weak [27] and no competition arises among J_1, J_4, and J_5, the origin for the small canting angle between the adjacent Fe1-Fe2 pair in the chain deserves further investigation. Inelastic neutron scattering and theoretical calculations are required to deter-

mine the strength of various interactions and figure out the origin for the small angle canting, while this clarification is beyond the scope of our work.

B. Magnetization behaviors

Given the magnetic transitions as revealed above, one is now able to check the anisotropic magnetization behaviors below T_N and T_1. Such anisotropy can be expected if one considers the lattice and magnetic symmetries of $Fe_4Nb_2O_9$. In fact, due to the triple rotational symmetry along the c axis, the [100] orientation in the P-3c1 phase is equivalent to the [010] and [-1-10] orientations, and correspondingly the perpendicular orientation is assigned as [120], [210], and [1-10], respectively. It was found that there exist three types of magnetic domains with equal population in zero magnetic field in $Co_4Nb_2O_9$ [32]. This equal population would be certainly broken if magnetic field was applied, and nonlinear magnetization which is attributed to a combined consequence of the alignment of magnetic domains and spin rotations would be observed. Considering the similarity of magnetic structure in $Co_4Nb_2O_9$ [32] and $Fe_4Nb_2O_9$ [28], it is thus expected that there exist three types of magnetic domains in $Fe_4Nb_2O_9$, in which the spins point along the [120], [210], and [1-10] directions, respectively, with equal population as $H = 0$. Obviously, the anisotropic magnetization can be expected from the spin alignment preference.

We present the measured $M(H)$ curves at several selected T, given H along the [1-10] and [001] directions, respectively, as shown in Figs. 3(c) and 3(d), confirming the anisotropy of M alignment. Indeed, the $M(H)$ curves along the [1-10] direction do exhibit the linear behavior in the low-H region, but significant deviation from the linear behavior in the high-H region is seen, and the field separating the two regions is called the critical field or threshold field H_c. The nonlinear deviation of $M(H)$ above H_c is most likely attributed to the realignment of the coexistent three types of magnetic domains into single domain, with their major magnetic moments perpendicular to H. While the critical field H_c is only 0.2 T for $Co_4Nb_2O_9$, it is as large as $H_c = 3$ T for $Fe_4Nb_2O_9$, implying that much stronger magnetic field is needed to realign magnetic domains. This is the reason why one observes the linear $M(H)$ behavior till $H \sim H_c \sim 3.0$ T or so for $Fe_4Nb_2O_9$. In addition, small deviation from the linear dependence for $M(H)$ along the [001] direction does not occur until very high H, suggesting that Fe^{2+} moments do not cant unless a high H is applied.

C. Magnetically induced electric polarization

We come now to investigate the ME effects of our $Fe_4Nb_2O_9$ crystals. Due to the complexity of domain structure, it is found that different orientation settings were used by different research groups. For instance, Ding *et al.* [28] and Zhang *et al.* [29] selected the [120]-oriented magnetic domain to investigate the ME coupling with x//[100], y//[120], while Jana *et al.* chose the [010] and [210] directions as the reference orientations [21]. Bearing in mind that the [1-10] orientation was previously used in $Co_4Nb_2O_9$ [22], which offers the same magnetic structure as $Fe_4Nb_2O_9$, we also chose the [1-10] orientation, whereas the magnetic moments antiferromagnetically aligned along the [1-10] direction. Here, we design x, y, and z axes along [1-10], [110], and [001] direction, respectively. Before discussing the measured data, it is worthy to address the data-processing issue when one applies this pyroelectric current technique. The sample was initially electrically and magnetically poled (ME poling) from $T = 120$ K down to $T = 10$ K with $+E = 6.67$ kV/cm and $-\mathrm{H} = -9$ T. It was seen that the collected pyroelectric current $I_T(T)$ curves each always show a relatively broad bump appearing around $T = 68$ K in all the cases. The bump at different sample warming rates demonstrated a considerably large shift ($\sim$5.5 K) toward the high-T side, indicating that this bump most likely originated from thermally stimulated depolarization current (TSDC) that was ascribed to the reorientation of charged dipoles or charge release. Certainly, no such shift occurred for the sharp peak emerging at T_N.

In fact, similar results were once reported in recent work [33]. The sources for such charges are the poling electric field that induced an internal depolarization field associated with the dipoles originating from frozen charge carriers. This internal field is opposite to the applied poling field since the relaxation time of these frozen dipoles is quite long at low T that these dipoles were robust and could persist during the long short-circuit procedure ($\sim$30 min). Therefore, when the sample was warmed up at a constant rate, the frozen dipoles were gradually released and contributed to the TSDC. The released current usually tends to increase exponentially first, reaches a threshold maximum, and then gradually drops to zero, forming a relatively broad pyroelectric current bump. In order to exclude the influence of TSDC, we first cooled the samples from 120 to 80 K with $E = 6.67$ kV/cm and $-H = -9$ T to fully align the ME domains, and then switched E to a much smaller value, $\sim$0.1 kV/cm at $T \sim 80$ K and below, to avoid the charge injection during the poling procedure. This method was confirmed to be effective, and the bump disappeared, allowing the pure pyroelectric current to be collected and processed.

Given the careful consideration of the measuring details, we now present the measured $I_T(T)$ curves along different directions, given a set of H along these orientations, respectively. For better illustration, we first present the measured $I_T(T)$ curves along the [110] direction at several selected H, as plotted in Figs. 4(a)–4(c), respectively. In the overall tendency, one sees the high-quality data, and the nine sets of data show remarkable difference from one another, indicating the strong anisotropy of the ME effect in this system. On the other hand, no identifiable $I_T(T)$ signals can be detected as $H = 0$ for all the cases, confirming the linear ME effect. Moreover, one sees that the collected $I_T(T)$ data along the [110] direction show strong dependence on H: not only on its magnitude but also on its direction, more evidence for magnetically induced electric polarization.

We first look at the dependence on direction of H. For a nonzero H along the [110] or [1-10] direction, the measured $I_T(T)$ along the [110] exhibits a sharp peak at T_N, followed by a shoulder below T_N with decreasing T. Further decreasing T leads to a clear sign reversal of $I_T(T)$ from positive value to negative one at $T = T_1$. The situation becomes very different as H is applied along the [001]. While the sharp peak at T_N is true, no signal reversal of the $I_T(T)$ data at T_1 has been identified and the current remained positive always. Second, we

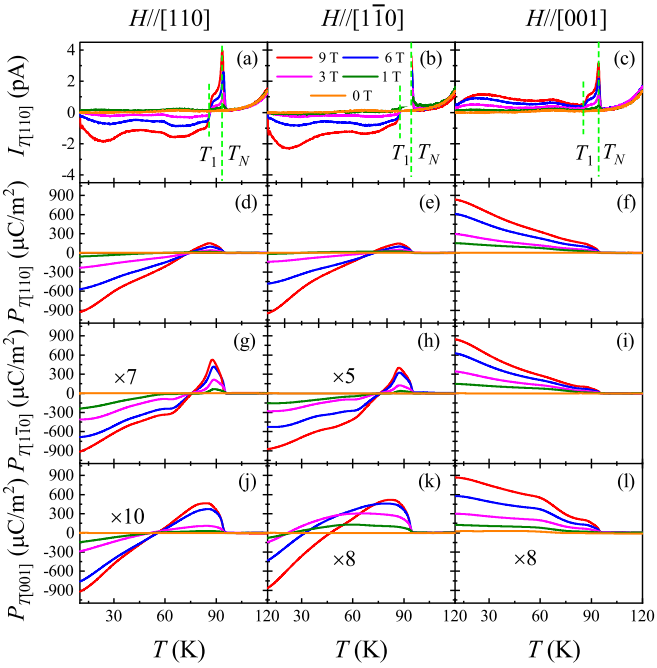

FIG. 4. Pyroelectric current $I_{[110]}$ as a function of temperature under different magnetic fields applied along (a) [110], (b) [1-10], and (c) [001] direction. (d)–(l) T dependence of polarization in the magnetic field and poling electric field applied along the [110], [1-10], and [001], alternatively. Green dashed lines indicate the magnetic transition points T_1 and T_N.

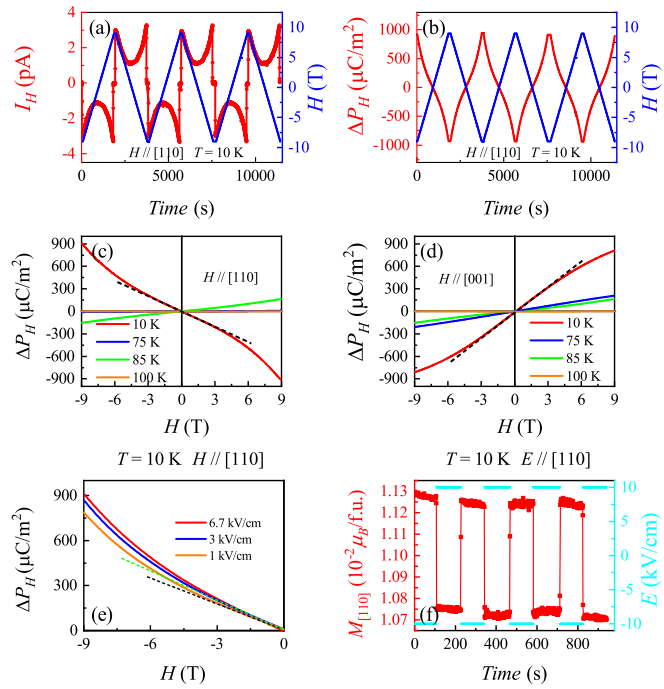

FIG. 5. (a) Magnetoelectric current I_H and (b) modulated field-induced polarization ΔP_H along [110] direction as a function of time with respect to linearly varying magnetic field between −9 and 9 T along [110] direction, respectively. (c) Corresponding H dependence of $\Delta P_{[110]}$ under H//[110] and (d) [001] direction, respectively. (e) H dependence of $\Delta P_{[110]}$ under different poling electric fields E at 10 K. (f) Modulated magnetization of $M_{[110]}$ as a function of external electric field E applied along [110] direction. Dashed lines are used to show the linear relationship.

discuss the dependence on magnitude of H. It is clear that the measured $I_T(T)$ is along the [110] direction and thus electric polarization P_T is induced by H, and qualitatively the higher H the larger $I_T(T)$, thus the larger $P_T(T)$ for all directions of H. The major concern for such magnitude dependences of current I_T and P_T includes their linearity or nonlinearity, associated with different ME physics. It will be seen that this dependence can be illustrated in another manner, i.e., the ME current I_H as a function of H at fixed T. We shall come back to this issue later.

Given the above overall description on the H dependences of electric polarization, now one can show all of the measured $P_T(T)$ data in the nine sets in terms of different (H, P_T) combinations, as shown in Figs. 4(d)–4(l). Several interesting features deserve highlighting here. First, the polarizations $P_T(T)$ along the [110], [1-10], and [001] directions, are all positive as long as magnetic field H is applied along the out-of-plane direction [001]. Second, when H is aligned along the [110] and [1-10] directions, respectively, the measured $P_T(T)$ emerging at T_N and below is positive and then a sign reversal appears at 75 K, below which the magnitude of $P_T(T)$ increases gradually with decreasing T. Third, the polarization is majorly aligned along the [110] direction and its magnitude is much larger than the values along the [1-10] and [001] directions, no matter which direction of H. It is confirmed that the magnetically induced electric polarization is highly anisotropic. In particular, the measured P_T at ∼10 K along the [110] direction reaches up to 900 μC/m^2 no matter which direction of the applied H ∼ 9 T. The largest polarization P in this $A_4M_2O_9$ family, together with the concomitant high-AFM transition point, makes $Fe_4Nb_2O_9$ attractive.

D. ME responses

Due to the magnetically induced electric polarization, we can now investigate systematically the ME responses, addressing the electric polarization response to H in the isothermal condition. The measurements of the ME responses, as described in the Sec. II, were performed mainly on the electric polarization along the [110] direction, since it is the largest. For the consideration of simplification, the isothermal ME current and polarization response are denoted as I_H and ΔP_H, and no more indication of the [110] direction is given unless stated elsewhere. The results will be presented in several different manners, as discussed below.

First, we measured $I_H(H)$ over the linear H cycling after the assigned poling process ($-H = -9$ T, $E = 6.67$ kV/cm). Figures 5(a) and 5(b) present the measured I_H and ΔP_H at $T = 10$ K, respectively, when H is applied along the [110] direction. The clear and instant response of $I_H(H)$ upon varying H is unambiguously demonstrated, as shown in Fig. 5(a). Such instant ME response can be more clearly seen from the evaluated $\Delta P_H(H)$, as shown in Fig. 5(b) where the antiphase response character is displayed with the opposite sign of $\Delta P_H(H)$ with respect to the sign of H, implying the negative ME coefficient $\alpha \sim (dP/dH) < 0$. It is seen that such

an antiphase response occurs only in the low-T range (e.g., $T \sim 10$ K) and the response becomes synchronous with H in the high-T range (e.g., $T \sim 85$ K), indicating the positive α, as shown in Fig. 5(c), while the magnitude of ΔP_H is remarkably reduced. When H was applied along the [001] direction, the ME responses over the whole T range below T_N were synchronous with $\alpha > 0$, as shown in Fig. 5(d).

Second and more interestingly, the ME response shows satisfactory linear character when H is low while it becomes remarkably nonlinear in the high-H region. The critical field H_c would be an important parameter for understanding the different mechanisms for the ME response. In proceeding, we look at the $\Delta P_H(H)$ data at $T = 10$ K, as shown in Fig. 5(e) where three sets of $\Delta P_H(H)$ data given different poling electric fields are plotted. It is seen that each of the three $\Delta P_H(H)$ curves does show the linear dependence in the low-H region and nonlinear dependence in the high-H region. Roughly, the as-obtained critical field is also $H_c \sim 3$ T, which coincides with the critical field for spin rotation and magnetic domain realignment, as shown in Fig. 3(c). This coincidence suggests the unique behavior of $Fe_4Nb_2O_9$ in terms of the ME response:

(i) Similar compound $Co_4Nb_2O_9$, which also exhibits the spin rotation and magnetic domain realignment at the critical field H_c, does not show any nonlinear ME response above H_c [22].

(ii) Earlier works demonstrated $Fe_4Nb_2O_9$ as a linear magnetoelectrics [29], while our results here uncover the nonlinear ME effect and electric polarization reversal by directly measuring the ME current.

In addition, as the other character of ME response, the possibility of electrically controlled magnetism was checked, as recently demonstrated for some linear ME materials [25,34,35]. Our results plotted in Fig. 5(f) show the [110]-oriented M in response to steplike electric field $E \sim \pm 10$ kV/cm applied along the [110] direction too. For this measurement, the sample was electrically poled from $T \sim 100$ to 10 K under $H = 2$ T and $E = 10$ kV/cm. After the sufficient short-circuit process, both H and E were set to zero, and subsequently M was collected in the presence of modulated E measuring $H \sim 0.2$ T along the [110] direction. Clearly, the measured M rapidly changed from $1.0725 \times 10^{-2}\ \mu_B$/f.u. at $E = 10$ kV/cm to $1.1246 \times 10^{-2}\ \mu_B$/f.u. at $E = -10$ kV/cm. It should be mentioned that no larger E applied to the sample could be allowed due to the limit of PPMS apparatus. Even so, the reverse ME coefficient defined as $\Delta M/\Delta E$ is ~ -25.1 ps/m.

E. ME manipulation

While the strong ME response has been demonstrated, it is more promising to check the ME intermanipulation. For the present case, the magnetically induced variation of electric polarization, $\Delta P_H(H)$, is closely related to the spin structure and magnetic anisotropy, which can be softly modulated through varying the magnetic field direction, an attractive model of ME manipulation, while the electrocontrol of variation in M, ΔM, has been evidenced [see Fig. 5(f)]. As the three magnetic domains realign into single one with their major spins perpendicular to the H, an important issue is how the in-plane electric polarization evolves upon variation of magnetic field direction below and above H_c. In order to clarify the relationship between the magnetic structure and induced electric polarization, we performed the measurements of ΔP_H along the [110] direction, in response to H rotating within the trigonal basal plane (rotating around the c axis).

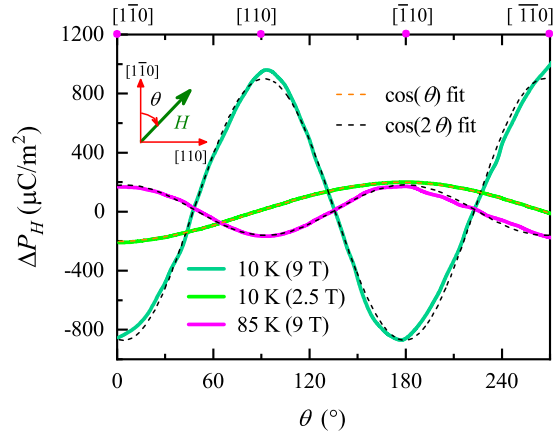

FIG. 6. Dependence of ΔP_H on angle θ defined by the relative direction of magnetic field H and the [1-10] axis at 10 K under $H = 9$ and 2.5 T as well as 85 K with $H = 9$ T.

The representative datasets are plotted in Fig. 6 where the angular dependence of ΔP_H on rotating H at $T = 10$ K and $T = 85$ K after the ME poling in the H//[1-10] and E//[110] configuration, respectively. On one hand, when H is larger than H_c, indicating the occurrence of field-induced spin rotation and magnetic domain realignment, a periodic variation of ΔP_H well fitted by term $\cos(2\theta)$ upon the rotation of $H = 9$ T at $T = 10$ K around the c axis can be observed. On the other hand, when H is smaller than H_c, e.g., $H = 2.5$ T, no such spin rotation and magnetic domain realignment would occur. It turns out that ΔP_H changes gradually synchronously in response of H rotating around the c axis.

Furthermore, when temperature is higher than the structural transition point but still below T_N ($\sim$93 K), e.g., $T = 85$ K, the periodic variation of ΔP_H can be also fitted by term $\cos(2\theta)$, but a $\pi/2$ phase shift of the response is identified. It is believed that all of these variations in angular-dependent electric polarization can be attributed to the modification of electric dipoles due to the direction of the Fe^{2+} magnetic moments mainly perpendicular to the magnetic field upon rotating the magnetic field, which will be discussed below.

F. ME phase diagrams

Our systematic investigations of the ME responses in $Fe_4Nb_2O_9$ allow a multiferroic phase diagram to be constructed which is H-orientation dependent. The phase diagrams for H aligned along the [110] and [001] directions are plotted in Figs. 7(a) and 7(b), respectively. Overall, the phase boundaries from measured data on various physical quantities are well consistent.

In Fig. 7(a), with H aligned along the [110] direction, $Fe_4Nb_2O_9$ accommodates four distinct major phases, labeled as high-temperature paraelectric and paramagnetic phase (PE, PM), ferroelectric and antiferromagnetic phase (FE1, AFM)

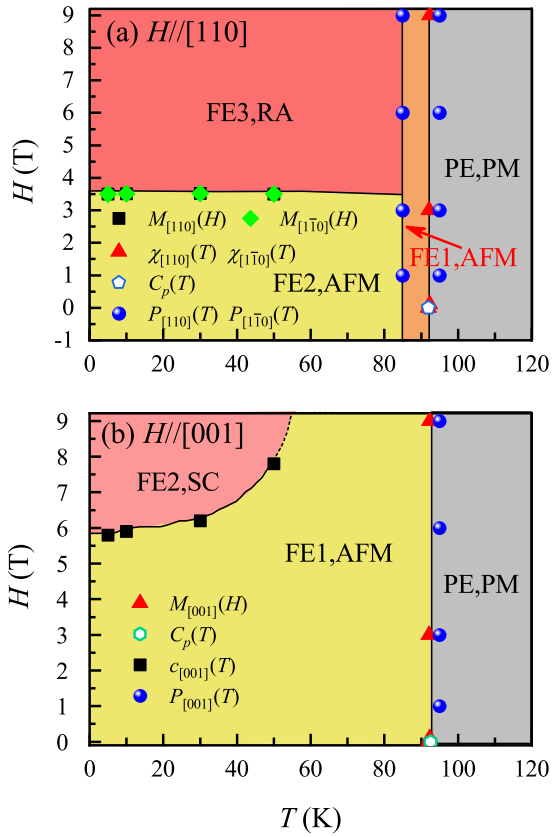

FIG. 7. (a) *H*-*T* phase diagrams of $Fe_4Nb_2O_9$ with magnetic field applied along [1-10], and (b) [001] direction.

between T_N and T_1, ferroelectric and antiferromagnetic phase (FE2, AFM) below T_1, and realignment of magnetic domains (FE3, RA). Here, the FE1 phase has positive polarization which decreases in magnitude and changes its sign in FE2 phase. Both FE1 and FE2 phases exhibit the linear ME response, whereas ΔP_H deviates from linearity in the FE3 phase.

In contrast, for *H*//[001], the phase diagram is plotted in Fig. 7(b) where three distinct multiferroic phases, labeled as (PE, PM), (FE1, AFM), and FE2, accompanied with spin canting (SC), are included. To this end, it can be inferred from the phase diagrams that magnetic domain realignment and spin canting have strong influence on the linear ME behavior, while the structure transition occurring at T_1 has significant influence on the modulation of ferroelectric domains.

IV. DISCUSSION

Given the aforementioned unique anisotropic ME effect and electric polarization reversal phenomena, it is thus important to discuss the microscopic mechanism of the ME coupling in $Fe_4Nb_2O_9$. Up to date, there are three most popular mechanisms to explain the magnetically induced ferroelectricity. In the spin current or inverse Dzyaloshinskii-Moriya (DM) mechanism, the induced ferroelectric polarization can be expressed as $\Delta p \propto e_{ij} \times (S_i \times S_j)$, where S_i and S_j are the spins of neighboring magnetic ions, and e_{ij} is the vector connecting the interacting neighbor spins [36]. Second, the ferroelectricity induced by the exchange striction mechanism can be expressed as $\Delta p \propto S_i \cdot S_j$ [37]. However, neither inverse DM mechanism nor exchange striction mechanism can work in Fe1 and Fe2 layers, since the sum of the vector spin chirality $S_i \times S_j$ in each honeycomb lattice is zero and the $S_i \cdot S_j$ is uniform for all Fe–Fe bonds in Fe1 and Fe2 layer. Finally, the metal-ligand hybridization *p*-*d* mechanism gives the local electric polarization $\Delta p \propto (S \cdot e_l)^2 e_l$ via the spin-orbit interaction, in which S is the moment of the transition-metal ion and e_l is the vector connecting the transition metal and the lth ligand [38]. Therefore, in the absence of the inversion symmetry at the transition-metal site, in terms of the local environment, a local dipole would be generated.

As the magnetic Fe^{2+} ion occupies a site with broken-inversion symmetry in $Fe_4Nb_2O_9$, the local dipole of the FeO_6 cluster can exist. In addition, it is worth noting that the induced electric polarization changing its direction upon rotating magnetic field was well explained using the metal-ligand hybridization *p*-*d* mechanism in $Co_4Nb_2O_9$ [39]. Therefore, based on the consideration mentioned above, we would like to give a tentative discussion to explain how the electric polarization emerges in the *ab* plane, why the structural transition accompanies electric polarization reversal, and concomitant ME coupling in $Fe_4Nb_2O_9$ using the metal-ligand hybridization *p*-*d* mechanism.

A. Local electric dipole of FeO_6 cluster

According to the metal-ligand *p*-*d* hybridization mechanism, the local dipole of the FeO_6 octahedral cluster can be expressed as $p \propto \sum_{l=1}^{6} (S \cdot e_l)^2 e_l$, where S is the magnetic moment of Fe ion, and e_l is the unit vector connecting the Fe and lth − ligand O ions, respectively. To obtain the expression of the local dipole $p = (p^x, p^y, p^z)$ in the FeO_6 octahedral cluster, we design x, y, and z axes along the [1-10], [110], and [001] direction. Since the symmetry of FeO_6 octahedron also changes when the structure phase transition occurs, the detailed local dipole expression in the *P*-3*c*1 and *C*2/*c* phase is given, respectively. In the *P*-3*c*1 phase, each FeO_6 octahedral cluster exhibits threefold rotational symmetry along z axis (3_z), and the six vectors e_{ij} along the Fe-O bonds in the polar coordinate can be expressed as

$$e_{11} = \begin{pmatrix} \sin\theta_1 \cos\varphi_1 \\ \sin\theta_1 \sin\varphi_1 \\ \cos\theta_1 \end{pmatrix},$$

$$e_{12} = \begin{pmatrix} \sin\theta_1 \cos(\varphi_1 + 2\pi/3) \\ \sin\theta_1 \sin(\varphi_1 + 2\pi/3) \\ \cos\theta_1 \end{pmatrix},$$

$$e_{13} = \begin{pmatrix} \sin\theta_1 \cos(\varphi_1 - 2\pi/3) \\ \sin\theta_1 \sin(\varphi_1 - 2\pi/3) \\ \cos\theta_1 \end{pmatrix},$$

$$e_{21} = \begin{pmatrix} \sin\theta_2 \cos\varphi_2 \\ \sin\theta_2 \sin\varphi_2 \\ \cos\theta_2 \end{pmatrix},$$

$$e_{22} = \begin{pmatrix} \sin\theta_2 \cos(\varphi_2 + 2\pi/3) \\ \sin\theta_2 \sin(\varphi_2 + 2\pi/3) \\ \cos\theta_2 \end{pmatrix},$$

$$e_{23} = \begin{pmatrix} \sin\theta_2 \cos(\varphi_2 - 2\pi/3) \\ \sin\theta_2 \sin(\varphi_2 - 2\pi/3) \\ \cos\theta_2 \end{pmatrix}, \quad (1)$$

where the index i denotes the oxygen positions, e.g., above ($i = 1$) and below ($i = 2$) the Fe ion, respectively. The index j denotes the threefold symmetric Fe-O bonds in the xy plane. Therefore, the local dipole p of FeO_6 octahedral cluster in the P-3c1 phase can be expressed as:

$$\begin{aligned}
p^x &\propto \mathrm{A}\sin^2\alpha\cos(-2\beta) + \mathrm{B}\sin^2\alpha\sin 2\beta + \mathrm{C}\sin 2\alpha\cos\beta, \\
p^y &\propto \mathrm{A}\sin^2\alpha\sin(-2\beta) + \mathrm{B}\sin^2\alpha\cos 2\beta + \mathrm{C}\sin 2\alpha\sin\beta, \\
p^z &\propto \mathrm{C_1}\sin^2\alpha + \mathrm{C_2}\cos^2\alpha, \\
\mathrm{A} &= \tfrac{3}{4}[\sin^3\theta_1(\cos^3\varphi_1 - 3\sin^2\varphi_1\cos\varphi_1) \\
&\quad + \sin^3\theta_2(\cos^3\varphi_2 - 3\sin^2\varphi_2\cos\varphi_2)], \\
\mathrm{B} &= \tfrac{3}{4}[\sin^3\theta_1(3\sin\varphi_1\cos^2\varphi_1 - \sin^3\varphi_1) \\
&\quad + \sin^3\theta_2(3\sin\varphi_2\cos^2\varphi_2 - \sin^3\varphi_2)], \\
\mathrm{C} &= \tfrac{3}{2}(\sin^2\theta_1\cos\theta_1 + \sin^2\theta_2\cos\theta_2), \\
\mathrm{C_1} &= 3(\sin^2\theta_1\cos\theta_1 + \sin^2\theta_2\cos\theta_2), \\
\mathrm{C_2} &= 3(\cos^3\theta_1 + \cos^3\theta_2) \qquad (2)
\end{aligned}$$

where A, B, C, C_1, and C_2 are the coupling constants correlated to the structural parameters of the FeO_6 octahedral cluster, α is the angle of the spin with respect to the z axis, and β is the corresponding angle of the projection of S on the xy plane with respect to the x axis. In contrast, due to the absence of 3_z symmetry, the local dipole $p = (p^x, p^y, p^z)$ in $C2/c$ phase can be expressed as:

$$\begin{aligned}
p^x &\propto \mathrm{A_1}\sin^2\alpha\cos^2\beta + \mathrm{A_2}\sin^2\alpha\sin^2\beta + \mathrm{A_3}\cos^2\alpha \\
&\quad + \mathrm{A_4}\sin^2\alpha\sin 2\beta + \mathrm{A_5}\sin 2\alpha\cos\beta + \mathrm{A_6}\sin 2\alpha\sin\beta \\
p^y &\propto \mathrm{A_4}\sin^2\alpha\cos^2\beta + \mathrm{B_2}\sin^2\alpha\sin^2\beta + \mathrm{B_3}\cos^2\alpha \\
&\quad + \mathrm{A_2}\sin^2\alpha\sin 2\beta + \mathrm{A_6}\sin 2\alpha\cos\beta + \mathrm{B_4}\sin 2\alpha\sin\beta \\
p^z &\propto \mathrm{C_1}\sin^2\alpha\cos^2\beta + \mathrm{C_2}\sin^2\alpha\sin^2\beta + \mathrm{C_3}\cos^2\alpha \\
&\quad + \mathrm{C_4}\sin^2\alpha\sin 2\beta + \mathrm{C_5}\sin 2\alpha\cos\beta + \mathrm{C_6}\sin 2\alpha\sin\beta \qquad (3)
\end{aligned}$$

Similarly, the coupling constants in Eq. (3) are also correlated to the structural parameters of FeO_6 octahedral cluster in $C2/c$ phase.

B. Spin-dependent electric polarization in $Fe_4Nb_2O_9$

We now consider the total electric polarization of the honeycomb lattice in Fe1 and Fe2 layer. As illustrated in Figs. 8(a)–8(d), the magnetic structures of the Fe1 and Fe2 layers can be represented by the two different sites S_1 and S_2. Each site consists of three identical magnetic ions forming a triangle. The local electric polarization $p_{S_1}(p_{S_2})$ can be obtained by the superposition of three local dipoles at the $S_1(S_2)$ site, while the electric polarization P_1 for the Fe1 layer and P_2 for the Fe2 layer can be obtained by the superposition of corresponding p_{S_1} and p_{S_2}. The total electric polarization P is the superposition of P_1 and P_2.

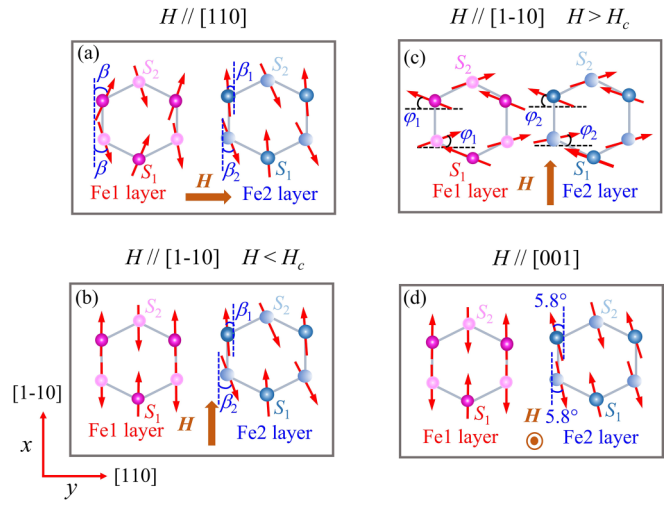

FIG. 8. Directions of the magnetic moment at the S_1 and S_2 sites in the Fe1 and Fe2 layer under the external magnetic field applied in (a) H//[110], (b) H//[1-10] and $H < H_c$, (c) H//[1-10] and $H > H_c$, and (d) H//[001]. Red arrows indicate the magnetic moments on each site. Blue and black dashed lines represent the x- and y directions. S_1 and S_2 represent the two Fe sites in each Fe1 and Fe2 layer.

In P-3c1 phase, the 3_z symmetry and three mirrors including [001] axis are allowed for each site, while the two sites are connected by the -1 and 2_y symmetry. When the Fe moments at the two sites are aligned along the $(\sin\alpha_{i_1}\cos\beta_{i_1},\ \sin\alpha_{i_1}\sin\beta_{i_1},\ \cos\alpha_{i_1})$ and $(\sin\alpha_{i_2}\cos\beta_{i_2},\ \sin\alpha_{i_2}\sin\beta_{i_2},\ \cos\alpha_{i_2})$ direction in the polar coordinate, respectively, after considering all the 3_z, 2_y, and -1 symmetry operations, the local electric polarization p_{S_1} and p_{S_2} can be expressed as, respectively,

$$p_{S1} \propto +3\begin{bmatrix} \mathrm{A}\sin^2\alpha_{i1}\cos 2\beta_{i1} + \mathrm{C}\sin 2\alpha_{i1}\cos\beta_{i_1} \\ \mathrm{A}\sin^2\alpha_{i_1}\sin(-2\beta_{i1}) + \mathrm{C}\sin 2\alpha_{i1}\sin\beta_{i1} \\ \mathrm{C_1}\sin^2\alpha_{i1} + \mathrm{C_2}\cos^2\alpha_{i1} \end{bmatrix},$$

$$p_{S2} \propto -3\begin{bmatrix} \mathrm{A}\sin^2\alpha_{i2}\cos 2\beta_{i2} + \mathrm{C}\sin 2\alpha_{i2}\cos\beta_{i_2} \\ \mathrm{A}\sin^2\alpha_{i2}\sin(-2\beta_{i_2}) + \mathrm{C}\sin 2\alpha_{i2}\sin\beta_{i2} \\ \mathrm{C_1}\sin^2\alpha_{i2} + \mathrm{C_2}\cos^2\alpha_{i2} \end{bmatrix}, \quad (4)$$

where $\alpha_{ij}(i,\ j = 1,\ 2)$ is the angle of the magnetic moment with respect to the z axis and $\beta_{ij}(i,\ j = 1,\ 2)$ is the corresponding angle of the projection of magnetic moment on the xy or ab plane with respect to the x axis. The index i denotes the honeycomb layer, e.g., $i = 1$ for the Fe1 layer and $i = 2$ for the Fe2 layer, and the index j denotes the magnetic site j in each honeycomb layer, e.g., $j = 1$ for the S_1 site and $j = 2$ for the S_2 site.

Here, it is worth pointing out that the Eq. (3) will change into Eq. (2) if we consider the 3_z symmetry of the FeO_6

cluster. In the P-3c1 phase, Eq. (3) relates the coupling constants by $A_1 = -A_2 = A$, $A_4 = -B_2 = B$, $A_3 = A_6 = B_3 = C_3 = C_4 = C_5 = C_6 = 0$, and $A_5 = B_4 = C$. Therefore, the first two terms in the expressions for p^x and p^y in Eq. (3) can be simplified as $\cos 2\beta$ and only three terms exist. Constrained by the 2_y symmetry, the term $A\sin^2\alpha \sin 2\beta$ in the x component of $p_{S_1}(p_{S_2})$ and the term $A\sin^2\alpha \cos 2\beta$ in the y component of $p_{S_1}(p_{S_2})$ cannot be considered anymore [39]. It thus implies that in the P-3c1 phase the x and y components of $p_{S_1}(p_{S_2})$ should mainly originate from the terms $A\sin^2\alpha \cos 2\beta$ and $A\sin^2\alpha \sin 2\beta$, respectively.

In contrast, as the O^{2-} ions shift in the ab plane, leading to the absence of 3_z symmetry in the FeO_6 cluster for the $C2/c$ phase, the relation $A_1 = -A_2$, $A_4 = -B_2$, $A_3 = A_6 = B_3 = C_3 = C_4 = C_5 = C_6 = 0$, and $A_5 = B_4$ are no longer applicable and six terms exist in the expressions for p^x and p^y. If we consider the term $A_4\sin^2\alpha \sin 2\beta$ in the x component of $p_{S_1}(p_{S_2})$ and term $A_2\sin^2\alpha\cos^2\beta + B_2\sin^2\alpha\sin^2\beta$ in the y component of $p_{S_1}(p_{S_2})$, the metal-ligand p-d hybridization mechanism would give rise to results inconsistent with our measured data. For example, in the case of H//[110], electric polarizations P_1, P_2 and total electric polarization P can be expressed as

$$P_1 \propto 6\begin{bmatrix} A_4 \sin 2\beta \\ A_2 \sin 2\beta \\ C_4 \sin 2\beta \end{bmatrix},$$

$$P_2 \propto 3\begin{bmatrix} A'_1(\cos^2\beta_1 - \cos^2\beta_2) + A'_2(\sin^2\beta_1 - \sin^2\beta_2) - A'_4(\sin 2\beta_1 - \sin 2\beta_2) \\ A'_4(\cos^2\beta_1 - \cos^2\beta_2) + B'_2(\sin^2\beta_1 - \sin^2\beta_2) - A'_2(\sin 2\beta_1 - \sin 2\beta_2) \\ C'_1(\cos^2\beta_1 - \cos^2\beta_2) + C'_2(\sin^2\beta_1 - \sin^2\beta_2) - C'_4(\sin 2\beta_1 - \sin 2\beta_2) \end{bmatrix},$$

$$P \propto 3\begin{bmatrix} A'_1(\cos^2\beta_1 - \cos^2\beta_2) + A'_2(\sin^2\beta_1 - \sin^2\beta_2) - A'_4(\sin 2\beta_1 - \sin 2\beta_2) + 2A_4 \sin 2\beta \\ A'_4(\cos^2\beta_1 - \cos^2\beta_2) + B'_2(\sin^2\beta_1 - \sin^2\beta_2) - A'_2(\sin 2\beta_1 - \sin 2\beta_2) + 2A_2 \sin 2\beta \\ C'_1(\cos^2\beta_1 - \cos^2\beta_2) + C'_2(\sin^2\beta_1 - \sin^2\beta_2) - C'_4(\sin 2\beta_1 - \sin 2\beta_2) + 2C_4 \sin 2\beta \end{bmatrix}. \quad (5)$$

It is clearly seen that the components P^x and P^y in both P_1 and P_2 are dominated by the terms $\sin 2\beta$ and $(\sin 2\beta_1 - \sin 2\beta_2)$, respectively. According to the crystal structural parameters obtained from the neutron powder diffraction at $T = 10$ K for the $C2/c$ phase [21], the coupling constants $A_2 = 0.0867$, $A_4 = -0.0923$, $A'_2 = 0.1182$, and $A'_4 = -0.265$ can be obtained, which indicate that $P_{[1\text{-}10]}$ is nearly two times larger than $P_{[110]}$, in contradiction with our experimental results that $P_{[110]}$ is much larger than $P_{[1\text{-}10]}$. In fact, such discrepancy is mainly due to the inclusion of term $A_4\sin^2\alpha \sin 2\beta$ in the x component of polarization $p_{S_1}(p_{S_2})$.

Honestly, the term $A_4 \sin^2\alpha \sin 2\beta$ in the x component of polarization $p_{S_1}(p_{S_2})$ and the term $A_4 \sin^2\alpha\cos^2\beta + B_2 \sin^2\alpha \sin^2\beta$ in the y component of polarization $p_{S_1}(p_{S_2})$ should be deleted and the x and y components of $p_{S_1}(p_{S_2})$ should also mainly originate from the terms $A_1 \sin^2\alpha\cos^2\beta + A_2 \sin^2\alpha \sin^2\beta$ and $A_2 \sin^2\alpha \sin 2\beta$ in the $C2/c$ phase, respectively, in order to reach the consistency between the formulas and the experimental data. Therefore, the local electric polarization p_{S_1} and p_{S_2} in the $C2/c$ phase can be simplified as

$$p_{S1} = 3\begin{bmatrix} A_1 \sin^2\alpha_{i1}\cos^2\beta_{i1} + A_2 \sin^2\alpha_{i1}\sin^2\beta_{i1} + A_3 \cos^2\alpha_{i1} \\ + A_5 \sin 2\alpha_{i1}\cos\beta_{i1} + A_6 \sin 2\alpha_{i1}\sin\beta_{i1} \\ B_3 \cos^2\alpha_{i1} + A_2 \sin^2\alpha_{i1}\sin 2\beta_{i1} \\ + A_6 \sin 2\alpha_{i1}\cos\beta_{i1} + B_4 \sin 2\alpha_{i1}\sin\beta_{i1} \\ C_1 \sin^2\alpha_{i1}\cos^2\beta_{i1} + C_2 \sin^2\alpha_{i1}\sin^2\beta_{i1} + C_3 \cos^2\alpha_{i1} \\ + C_4 \sin^2\alpha 1 \sin 2\beta_{i1} + C_5 \sin 2\alpha_{i1}\cos\beta_{i1} + C_6 \sin 2\alpha_{i1}\sin\beta_{i1} \end{bmatrix},$$

$$p_{S2} = -3\begin{bmatrix} A_1 \sin^2\alpha_{i2}\cos^2\beta_{i2} + A_2 \sin^2\alpha_{i2}\sin^2\beta_{i2} + A_3 \cos^2\alpha_{i2} \\ + A_5 \sin 2\alpha_{i2}\cos\beta_{i2} + A_6 \sin 2\alpha_{i2}\sin\beta_{i2} \\ B_3 \cos^2\alpha_{i2} + A_2 \sin^2\alpha_{i2}\sin 2\beta_{i2} \\ + A_6 \sin 2\alpha_{i2}\cos\beta_{i2} + B_4 \sin 2\alpha_{i1}\sin\beta_{i2} \\ C_1 \sin^2\alpha_{i2}\cos^2\beta_{i_2} + C_2 \sin^2\alpha_{i2} \sin^2\beta_{i2} + C_3 \cos^2\alpha_{i2} \\ + C_4 \sin^2\alpha_{i2} \sin 2\beta_{i2} + C_5 \sin 2\alpha_{i2} \cos\beta_{i2} + C_6 \sin 2\alpha_{i2} \sin\beta_{i2} \end{bmatrix}. \quad (6)$$

Given the above discussion, we shall use Eq. (4) and Eq. (6) to explain the magnetically induced ferroelectric polarization, the electric polarization reversal upon the structural phase transition from high-T P-3c1 phase to the low-T $C2/c$ phase, as well as the dependence of polarization on the direction of magnetic field.

C. Magnetic field-driven ferroelectric polarization reversal based on *p-d* hybridization mechanism

In fact, as shown in Figs. 1(b)–1(e), the magnetic symmetries of the Fe1 and Fe2 layers are different from each other, due to a small canting angle of 5.81°. In this case, based on the symmetry analysis [40,41], the Fe2 layer in the P-3c1 phase has an independent $-1'$ symmetry, while the Fe1 layer exhibits the symmetry described by $2/m'$ plus $-1'$ symmetry, where symbol 2 marks the twofold symmetry axis along [110], and m' is the mirror symmetry perpendicular to the [110] direction plus a time-reversal symmetry. In the $C2/c$ phase, the magnetic structures of the Fe1 and Fe2 layers both satisfy the $-1'$ symmetry. Due to the presence of the $-1'$ symmetry, the electric polarizations p_{S_1} and p_{S_2} in the Fe1 and Fe2 layers are canceled with each other and no electric polarization is available. However, the applied magnetic field will break the $-1'$ symmetry, resulting in nonzero P_1 and P_2 aligned along some direction in space. Similar conclusion can be also obtained from Eq. (4) and Eq. (6), as the magnetic moments at the S_1 and S_2 sites in the Fe1 and Fe2 layers are antiparallel in the absence of magnetic field. However, in the case of H//[110], as presented in Fig. 8(a), relations $\alpha_{11} = \alpha_{12} = 90°$, $\beta_{11} = \beta$, and $\beta_{12} = \pi - \beta$ are satisfied in the Fe1 layer, while relations $\alpha_{21} = \alpha_{22} = 90°$, $\beta_{21} = -\beta_1$, and $\beta_{22} = \pi - \beta_2$ are satisfied in the Fe2 layer. Consequently, the electric polarizations P_1 and P_2, and total electric polarization P can be expressed as

$$
\begin{aligned}
P_1 &\propto 6\mathrm{A}\begin{bmatrix} 0 \\ -\sin 2\beta \\ 0 \end{bmatrix}, \\
P_2 &\propto 3\mathrm{A}'\begin{bmatrix} \cos 2\beta_1 - \cos 2\beta_2 \\ \sin 2\beta_1 - \sin 2\beta_2 \\ 0 \end{bmatrix}, \\
P &= \begin{bmatrix} P^x \\ P^y \\ P^z \end{bmatrix} \propto 3\begin{bmatrix} \mathrm{A}'(\cos 2\beta_1 - \cos 2\beta_2) \\ \mathrm{A}'(\sin 2\beta_1 - \sin 2\beta_2) - 2\mathrm{A}\sin 2\beta \\ 0 \end{bmatrix},
\end{aligned} \tag{7}
$$

where A and A' are the coupling constants of the S_1 site in the Fe1 and Fe2 layers, respectively.

We can see that nonzero electric polarization components $P^x(P_{T[1\text{-}10]})$ and $P^y(P_{T[110]})$ can be induced by magnetic field H applied along the [110] direction. According to the crystal structural parameters obtained from the neutron powder diffraction at $T = 150$ K [21], coupling constants $\mathrm{A} = 0.0156$ and $\mathrm{A}' = 0.1818$ can be obtained, indicating that the magnetically induced polarization in the P-3c1 phase is mainly from the Fe2 layer, due to the larger lattice distortion of the $(Fe_2)O_6$ octahedron. Therefore, polarization P^y is larger than P^x, as deduced from Eq. (7), well consistent with our experimental data as shown in Fig. 4.

On the other side, in the case of $C2/c$ phase, electric polarizations P_1 and P_2, and total electric polarization P can be obtained as

$$
\begin{aligned}
P_1 &\propto 6\begin{bmatrix} 0 \\ \mathrm{A}_2 \sin 2\beta \\ \mathrm{C}_4 \sin 2\beta \end{bmatrix}, \\
P_2 &\propto 3\begin{bmatrix} \mathrm{A}'_1(\cos^2\beta_1 - \cos^2\beta_2) + \mathrm{A}'_2(\sin^2\beta_1 - \sin^2\beta_2) \\ \text{-}\mathrm{A}'_2(\sin 2\beta_1 - \sin 2\beta_2) \\ \mathrm{C}'_1(\cos^2\beta_1 - \cos^2\beta_2) + \mathrm{C}'_2(\sin^2\beta_1 - \sin^2\beta_2) \\ -\mathrm{C}'_4(\sin 2\beta_1 - \sin 2\beta_2) \end{bmatrix}, \\
P &= \begin{bmatrix} P^x \\ P^y \\ P^z \end{bmatrix} \propto 3\begin{bmatrix} \mathrm{A}'_1(\cos^2\beta_1 - \cos^2\beta_2) + \mathrm{A}'_2(\sin^2\beta_1 - \sin^2\beta_2) \\ \text{-}\mathrm{A}'_2(\sin 2\beta_1 - \sin 2\beta_2) + 2\mathrm{A}_2 \sin 2\beta \\ \mathrm{C}'_1(\cos^2\beta_1 - \cos^2\beta_2) + \mathrm{C}'_2(\sin^2\beta_1 - \sin^2\beta_2) \\ -\mathrm{C}'_4(\sin 2\beta_1 - \sin 2\beta_2) + 2\mathrm{C}_4 \sin 2\beta \end{bmatrix},
\end{aligned} \tag{8}
$$

where A_2, C_4 are the coupling constants of the S_1 site in the Fe1 layer, and A'_1, A'_2, C'_1, C'_2, C'_4 are the coupling constants of the S_1 site in the Fe2 layer. Similarly, the aforementioned coupling constants $\mathrm{A}_2 = -0.005$, $\mathrm{C}_4 = 0.012$, $\mathrm{A}'_1 = -0.1861$, $\mathrm{A}'_2 = 0.1182$, $\mathrm{C}'_1 = 0.0252$, $\mathrm{C}'_2 = 0.09$, and $\mathrm{C}'_4 = -0.045$ can be extracted by using the previously reported crystal structural parameters at $T = 10$ K [21].

It is found that the largest polarization also comes from the Fe2 layer, and the electric polarization is aligned mainly along the [110] direction, similar to the case of the P-3c1 phase. However, here for the $C2/c$ phase, the polarization components P^x and P^y will change their sign, according to Eq. (7) and Eq. (8). For example, substituting the coupling constants into Eq. (7) and Eq. (8), respectively, we obtain that $P^x = -1.091\sin(\beta_1 - \beta_2)\sin(\beta_1 + \beta_2)$ in the P-3c1 phase and $P^x = 0.913\sin(\beta_1 - \beta_2)\sin(\beta_1 +$

β_2) in the $C2/c$ phase, respectively, while $P^y = 1.091\sin(\beta_1 - \beta_2)\cos(\beta_1 + \beta_2)$ in the P-3c1 phase and $P^y = -0.7092\sin(\beta_1 - \beta_2)\cos(\beta_1 + \beta_2)$ in the $C2/c$ phase. It is thus clearly demonstrated that P^y is larger than P^x and P^x (P^y) in the P-3c1 phase and $C2/c$ phase are always opposite to each other, well consistent with our experimental results.

Here it should be pointed out that in our experiments the magnitude of electric polarization P^y in the $C2/c$ phase is larger than that in the P-3c1 phase. However, according to Eq. (7) and Eq. (8), the magnitude of P^y in the $C2/c$ phase is smaller than that in the P-3c1 phase, and this discrepancy may be due to the larger leakage in the measurement carried at high $T \sim 85$ K, leading to the issue that electric dipoles may not be well aligned.

In addition, we can also obtain $P^z \propto 0.27\sin(\beta_1 - \beta_2)\cos(\beta_1 + \beta_2)$ in the $C2/c$ phase, significantly smaller than P^y, also in agreement with the experimental results. Here, it is worth noting that the angles β, β_1, and β_2 for the two phases should be slightly different, but we indeed do not distinguish these small differences for simplicity, and the main conclusion should not be affected.

Subsequently, we consider the case of H//[1-10]. As presented in Fig. 8(b), for $H < H_c$, $\alpha_{11} = \alpha_{12} = 90^\circ$, $\beta_{11} = 0^\circ$, $\beta_{12} = 180^\circ$, which indicate that P_1 is always zero no matter in the P-3c1 phase or $C2/c$ phase, consistent with the symmetry analysis. In contrast, the angles in the Fe_2 layer can be expressed as $\alpha_{21} = \alpha_{22} = 90^\circ$, $\beta_{21} = -\beta_1$, and $\beta_{22} = 180^\circ - \beta_2$; thus, the total polarization (P) in the P-3c1 phase and $C2/c$ phase can be formulated in the following Eq. (9) and Eq. (10), respectively:

$$P = P_2 \propto 3\mathrm{A}'\begin{bmatrix}\cos 2\beta_1 - \cos 2\beta_2\\ -\sin 2\beta_2 + \sin 2\beta_1\\ 0\end{bmatrix}, \tag{9}$$

$$P = P_2 \propto 3\begin{bmatrix}\mathrm{A}_1'(\cos^2\beta_1 - \cos^2\beta_2) + \mathrm{A}_2'(\sin^2\beta_1 - \sin^2\beta_2)\\ -\mathrm{A}_2'(\sin 2\beta_1 - \sin 2\beta_2)\\ \mathrm{C}_1'(\cos^2\beta_1 - \cos^2\beta_2) + \mathrm{C}_2'(\sin^2\beta_1 - \sin^2\beta_2)\\ -\mathrm{C}_4'(\sin 2\beta_1 - \sin 2\beta_2)\end{bmatrix}. \tag{10}$$

It is clearly seen that the polarization in the $C2/c$ phase shows nonzero components along all the x-, y-, and z directions, consistent with the experimental results. In particular, the electric polarization along the y axis reverses its sign upon the structural transition from the P-3c1 to the $C2/c$ phase. When $H > H_c$, accompanied with the reoriented spins and realigned three types of magnetic domains, the spins are mainly perpendicular to the magnetic field with the canting angle $\varphi_1(\varphi_2)$ toward y or [110] direction, as illustrated Fig. 8(c). The corresponding polarizations in the P-3c1 phase and $C2/c$ phase can be written as Eq. (11) and Eq. (12), respectively:

$$P_1 \propto 6\mathrm{A}\begin{bmatrix}0\\ -\sin 2\varphi_1\\ 0\end{bmatrix},$$

$$P_2 \propto 6\mathrm{A}'\begin{bmatrix}0\\ -\sin 2\varphi_2\\ 0\end{bmatrix},$$

$$P = \begin{bmatrix}P^x\\ P^y\\ P^z\end{bmatrix} \propto 6\begin{bmatrix}0\\ -\mathrm{A}\sin 2\varphi_1 - \mathrm{A}'\sin 2\varphi_2\\ 0\end{bmatrix} \tag{11}$$

$$P_1 \propto 6\begin{bmatrix}0\\ \mathrm{A}_2\sin 2\varphi_1\\ \mathrm{C}_4\sin 2\varphi_1\end{bmatrix},\ P_2 \propto 6\begin{bmatrix}0\\ \mathrm{A}_2'\sin 2\varphi_2\\ \mathrm{C}_4'\sin 2\varphi_2\end{bmatrix},$$

$$P = \begin{bmatrix}P^x\\ P^y\\ P^z\end{bmatrix} \propto 6\begin{bmatrix}0\\ \mathrm{A}_2\sin 2\varphi_1 + \mathrm{A}_2'\sin 2\varphi_2\\ \mathrm{C}_4\sin 2\varphi_1 + \mathrm{C}_4'\sin 2\varphi_2\end{bmatrix}. \tag{12}$$

Similarly, in this case, it is clearly seen that the polarizations along the y axis in the P-3c1 and $C2/c$ phases are still opposite to each other, and the polarization along the z axis is much smaller than that along the y axis.

Furthermore, when H is applied along the [001] direction, as shown in Fig. 8(d), the moments in the three types of magnetic domains will tilt a little bit to the external field, namely $\alpha_{i_1} = \alpha$, $\alpha_{i_2} = -\alpha$, implying that the in-plane spins are still aligned antiparallel to each other. Therefore, no net electric polarization can be generated in the P-3c1 phase or $C2/c$ phase by the metal ligand p-d hybridization mechanism, implying that another unknown mechanism plays a role here. It is worth reminding that while the polarization induced by magnetic field along the [110] and [1-10] directions mainly originate from the spin-dependent p-d hybridization mechanism, the polarization induced by magnetic field along the z direction is believed to originate from other mechanisms, and thus different T-dependent behaviors for magnetic field-induced polarization can be expected.

Honestly, there exist two more questions regarding the p-d hybridization mechanism to be addressed. First, the p-d hybridization mechanism does not predict nonzero polarization along the x or [1-10] direction, when H is applied along the [1-10] direction with $H > H_c$, according to Eq. (11) and Eq. (12). Unfortunately, in this work we indeed observed nonzero polarization which should not be treated as measuring uncertainties. Such an inconsistency can be reasonably understood as three types of magnetic domains in $Fe_4Nb_2O_9$ are not fully realigned into a single one, and the other two types of magnetic domains still exist, as the magnetization $M_{[1\text{-}10]}(H)$ exhibits the nonlinear behavior. In this case, similar to the situation in the Fe2 layer, the magnetic moments at the S_1 and

S_2 sites in the other two magnetic domains will form different angles with respect to the x axis, giving rise to nonzero P^x, according to Eq. (4) and Eq. (6). However, we have no direct evidence for this explanation and the question remains to be confirmed.

The second question is that no z-component electric polarization can be generated in the P-3c1 phase by the p-d hybridization mechanism when H is applied in the xy plane, while a finite polarization is always experimentally observed, no matter along which direction the magnetic field is applied. As shown in Figs. 4(j)–4(k), the crossing points of $P_{T_{[001]}}$ exhibit quite different features compared to $P_{[110]}$ and $P_{[1\text{-}10]}$, implying that $P_{T_{[001]}}$ may be induced by other mechanisms to be discussed briefly here.

First, the inverse DM mechanism gives the electric dipole $\Delta p \propto e_{ij} \times (S_i \times S_j)$ at the bond between sites i and j lying in the xy plane and $P_{T_{[001]}}$ cannot be expected from this mechanism. Second, as shown in Fig. 1(a), there are two $(Fe1)O_6/(Fe2)O_6$ dimers connected by the -1 symmetry in the unit cell of $Fe_4Nb_2O_9$. Since the Fe^{2+} ions are in nonequivalent environment with different rigidities, and the charges of Fe1 and Fe2 ions may be slightly different, the $(Fe1)O_6/(Fe2)O_6$ dimer may give different dipole moments. Therefore, the local electric dipole is modified by the scalar product of neighboring magnetic moments, namely exchange striction mechanism as the magnetic structure changes in response to an applied magnetic field. In the ground state of P-3c1 phase, the variation of the dipoles in $(Fe1)O_6/(Fe2)O_6$ dimer will be canceled out due to the same angle between the moments of Fe1 and Fe2 ions. However, applying H along the [110] and a finite $H < H_c$ along [1-10] direction will cause the different angles between the moments of Fe1 and Fe2 ions, as shown in Figs. 8(a) and 8(b), giving rise to a net electric polarization $P_{T_{[001]}}$. When a large $H > H_c$ is applied along the [1-10] direction, the magnetic structures of Fe1 and Fe2 layers are realigned to be identical, as shown in Fig. 8(c). However, the magnetic moments on the S_1 and S_2 sites in the other two magnetic domains will form different angles with respect to the x axis, and thus nonzero net electric polarization can be generated from exchange striction mechanism. In the $C2/c$ phase, the z components of electric polarization can be expected by the spin-dependent p-d mechanism while the exchange striction mechanism may also work, and under the different magnitudes of magnetic field the electric polarization $P_{T_{[001]}}$ induced by more than one mechanism may be possible at different points, especially for H//[1-10] direction. Further investigation is motivated to elucidate the microscopic origin of electric polarization $P_{T_{[001]}}$ in $Fe_4Nb_2O_9$, while a tentative discussion is given based on the aforementioned two mechanisms and experimental results.

Finally, we would like to explain the ME response to H rotating along the z axis. In the AFM phase, the magnetically induced polarization ΔP_H can be expressed as $\Delta P_H \propto \alpha H \cos\theta$, where θ denotes the angle measured from x- or [1-10] direction. Indeed, ΔP_H changes synchronously in response to H rotating around the z axis, shown in Fig. 6. When $H > H_c$ is applied along the [1-10] direction, as shown in Fig. 9, accompanied with the reoriented spins and realigned three types of magnetic domains, the moments are mainly perpendicular to H. When H is rotated by an angle θ around the z axis, all the moments will be rotated by angle θ to be aligned perpendicular to H, and thus the ΔP_H in the P-3c1 and $C2/c$ phase can be expressed in the following Eqs. (13) and Eq. (14), respectively, where $\alpha_{11} = \alpha_{12} = 90°$, $\beta_{11} = -90° + \varphi_1 + \theta$, $\beta_{12} = 90° - \varphi_1 + \theta$ in the Fe1 layer, while $\alpha_{21} = \alpha_{22} = 90°$, $\beta_{21} = -90° + \varphi_2 + \theta$, $\beta_{22} = 90° - \varphi_2 + \theta$:

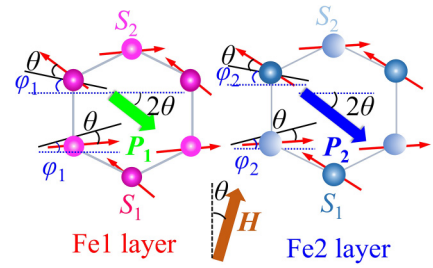

FIG. 9. Correlation among the magnetic field direction, the magnetic structure, and the induced polarization of Fe1 and Fe2 layer under a magnetic field applied in the ab plane rotation at 85 K. $\varphi_1(\varphi_2)$ is the canting angle of the magnetic moments for Fe1(Fe2) layer under H//[1-10]. θ is the angle of H measured from [1-10] direction. Blue dashed lines denote the x direction and the black solid lines denote the original location of moments for H//[1-10].

$$\Delta P_H \propto -6[\mathrm{A}\sin 2\varphi_1 + \mathrm{A}'\sin 2\varphi_2]\cos(-2\theta), \tag{13}$$

$$\Delta P_H \propto 6(\mathrm{A}_2\sin 2\varphi_1 + \mathrm{A}'_2\sin 2\varphi_2)\cos(-2\theta). \tag{14}$$

It is clearly seen that in both the P-3c1 phase and $C2/c$ phase the electric polarization ΔP_H indeed varies with $\cos(-2\theta)$, well consistent with our experimental results. Similarly, due to the opposite sign of the coefficients of $\cos(-2\theta)$ terms in the P-3c1 and $C2/c$ phase, a 90° phase shift for ΔP_H measured at 85 and 10 K can be observed.

V. CONCLUSION

In summary, we have systematically investigated the ME coupling effect in single-crystalline $Fe_4Nb_2O_9$. Using the metal-ligand p-d hybridization mechanism, the magnetically induced ferroelectric polarization, the electric polarization reversal upon the structural phase transition from high-T P-3c1 phase to the low-T $C2/c$ phase, as well as the dependence of polarization on the direction of magnetic field, can be well explained. Based on the coupling constants obtained from the structure parameters of P-3c1 phase at 150 K and $C2/c$ phase at 10 K, it is revealed that the magnetically induced electric polarization mainly originates from Fe2 layers. While the polarization induced by magnetic field along the [110] and [1-10] directions mainly originate from the spin-dependent p-d hybridization mechanism, the polarization induced by magnetic field along the z direction is believed to originate from other mechanisms, and thus different T-dependent behaviors for magnetic field-induced polarization can be observed. In addition, as the symmetry of crystal structure changes from trigonal P-3c1 to monoclinic $C2/c$, the changes of parameters

of FeO_6 octahedral cluster modulate the strength of magnitude of polarization of Fe1 and Fe2 sublattices, thereby interpreting the electric polarization changes and concomitant ME coupling effect. Our work may pave the way for understanding the magnetoelectric mechanism in the presence of rich phase diagram in this $A_4M_2O_9$ family.

ACKNOWLEDGMENT

The authors would like to acknowledge the financial support from the National Natural Science Foundation of China (Grants No. 92163210, No. 12274231, No. 11874031, No. 11834002, No. 12074111, No. 51721001, No. 52272108, and No. 11974167).

[1] S.-W. Cheong and M. Mostovoy, Multiferroics: A magnetic twist for ferroelectricity, Nat. Mater. **6**, 13 (2007).
[2] A. S. Zimmermann, D. Meier, and M. Fiebig, Ferroic nature of magnetic toroidal order, Nat. Commun. **5**, 4796 (2014).
[3] S. Dong, J.-M. Liu, S.-W. Cheong, and Z. F. Ren, Multiferroic materials and magnetoelectric physics: Symmetry, entanglement, excitation, and topology, Adv. Phys. **64**, 519 (2015).
[4] T. Choi, Y. Horibe, H. T. Yi, Y. J. Choi, Weida Wu, and S.-W. Cheong, Insulating interlocked ferroelectric and structural antiphase domain walls in multiferroic $YMnO_3$, Nat. Mater. **9**, 253 (2010).
[5] Y. Tokura and S. Seki, Multiferroics with spiral spin orders, Adv. Mater. **22**, 1554 (2010).
[6] N. A. Spaldin and R. Ramesh, Advances in magnetoelectric multiferroics, Nat. Mater. **18**, 203 (2019).
[7] C. L. Lu, M. H. Wu, L. Lin, and J.-M. Liu, Single-phase multiferroics: New materials, phenomena, and physics, Natl. Sci. Rev. **6**, 653 (2019).
[8] S. Ghosh, H. Das, and C. J. Fennie, Linear magnetoelectricity at room temperature in perovskite superlattices by design, Phys. Rev. B **92**, 184112 (2015).
[9] J. Ma, J. Hu, Z. Li, and C. W. Nan, Recent progress in multiferroic magnetoelectric composites: From bulk to thin films, Adv. Mater. **23**, 1062 (2011).
[10] F. Matsukura, Y. Tokura, and H. Ohno, Control of magnetism by electric fields, Nat. Nanotechnol. **10**, 209 (2015).
[11] L. Weymann, L. Bergen, T. Kain, A. Pimenov, A. Shuvaev, E. Constable, D. Szaller, B. V. Mill, A. M. Kuzmenko, V. Y. Ivanov, N. V. Kostyuchenko, A. I. Popov, A. K. Zvezdin, A. Pimenov, A. A. Mukhin, and M. Mostovoy, Unusual magnetoelectric effect in paramagnetic rare-earth langasite, npj Quant. Mater. **5**, 61 (2020).
[12] A. Iyama and T. Kimura, Magnetoelectric hysteresis loops in Cr_2O_3 at room temperature, Phys. Rev. B **87**, 180408(R) (2013).
[13] I. Kornev, M. Bichurin, J.-P. Rivera, S. Gentil, H. Schmid, A. G. M. Jansen, and P. Wyder, Magnetoelectric properties of $LiCoPO_4$ and $LiNiPO_4$, Phys. Rev. B **62**, 12247 (2000).
[14] G. Z. Zhou, J. W. Gong, X. Li, M. F. Liu, L. Y. Li, Y. Wang, J. H. Min, J. Liu, D. Cai, F. Liu, S. H. Zheng, Y. S. Tang, Z. C. Xu, Y. L. Xie, L. Yang, M. Zeng, Z. Y. Yan, B. W. Li, X. Z. Wang, and J.-M. Liu, Large magnetoelectric effect in the polar magnet Sm_2BaCuO_5, Appl. Phys. Lett. **115**, 252902 (2019).
[15] K. Yoo, B. Koteswararao, J. Kang, A. Shahee, W. Nam, F. F. Balakirev, V. S. Zapf, N. Harrison, A. Guda, N. Ter-Oganessian, and K. H. Kim, Magnetic field-induced ferroelectricity in $S = 1/2$ kagome staircase compound $PbCu_3TeO_7$, npj Quant. Mater. **3**, 45 (2018).
[16] T. Kurumaji, S. Ishiwata, and Y. Tokura, Doping-Tunable Ferrimagnetic Phase with Large Linear Magnetoelectric Effect in a Polar Magnet $Fe_2Mo_3O_8$, Phys. Rev. X **5**, 031034 (2015).
[17] Y. Wang, G. L. Pascut, B. Gao, T. A. Tyson, K. Haule, V. Kiryukhin, and S. W. Cheong, Unveiling hidden ferrimagnetism and giant magnetoelectricity in polar magnet $Fe_2Mo_3O_8$, Sci. Rep. **5**, 12268 (2015).
[18] S. Seki, S. Ishiwata, and Y. Tokura, Magnetoelectric nature of skyrmions in a chiral magnetic insulator Cu_2OSeO_3, Phys. Rev. B **86**, 060403(R) (2012).
[19] Y. Tokunaga, N. Furukawa, H. Sakai, Y. Taguchi, T. H. Arima, and Y. Tokura, Composite domain walls in a multiferroic perovskite ferrite, Nat. Mater. **8**, 558 (2009).
[20] A. Maignan and C. Martin, $Fe_4Nb_2O_9$: A magnetoelectric antiferromagnet, Phys. Rev. B **97**, 161106(R) (2018).
[21] R. Jana, D. Sheptyakov, X. Y. Ma, J. A. Alonso, M. C. Pi, A. Muñoz, Z. Y. Liu, L. L. Zhao, N. Su, S. F. Jin, X. B. Ma, K. Sun, D. F. Chen, S. Dong, Y. S. Chai, S. L. Li, and J. G. Cheng, Low-temperature crystal and magnetic structures of the magnetoelectric material $Fe_4Nb_2O_9$, Phys. Rev. B **100**, 094109 (2019).
[22] N. D. Khanh, N. Abe, H. Sagayama, A. Nakao, T. Hanashima, R. Kiyanagi, Y. Tokunaga, and T. Arima, Magnetoelectric coupling in the honeycomb antiferromagnet $Co_4Nb_2O_9$, Phys. Rev. B **93**, 075117 (2016).
[23] Y. Cao, G. Deng, P. Beran, Z. Feng, B. Kang, J. Zhang, N. Guiblin, B. Dkhil, W. Ren, and S. X. Cao, Nonlinear magnetoelectric effect in paraelectric state of $Co_4Nb_2O_9$ single crystal, Sci. Rep. **7**, 14079 (2017).
[24] S. Choi, D. G. Oh, M. J. Gutmann, S. Pan, G. Kim, K. Son, J. Kim, N. Lee, S. W. Cheong, Y. J. Choi, and V. Kiryukhin, Noncollinear antiferromagnetic order in the buckled honeycomb lattice of magnetoelectric $Co_4Ta_2O_9$ determined by single-crystal neutron diffraction, Phys. Rev. B **102**, 214404 (2020).
[25] S. H. Zheng, G. Z. Zhou, X. Li, M. F. Liu, Y. S. Tang, Y. L. Xie, M. Zeng, L. Lin, Z. B. Yan, X. K. Huang, X. P. Jiang, and J. M. Liu, Remarkable magnetoelectric effect in single crystals of honeycomb magnet $Mn_4Nb_2O_9$, Appl. Phys. Lett. **117**, 072903 (2020).
[26] S. N. Panja, P. Manuel, and S. Nair, Anisotropy in the magnetization and magnetoelectric response of single crystalline $Mn_4Ta_2O_9$, Phys. Rev. B **103**, 014422 (2021).
[27] G. C. Deng, Y. M. Cao, W. Ren, S. X. Cao, A. J. Studer, N. Gauthier, M. Kenzelmann, G. Davidson, K. C. Rule, J. S. Gardner, P. Imperia, C. Ulrich, and G. J. McIntyre, Spin dynamics and magnetoelectric coupling mechanism of $Co_4Nb_2O_9$, Phys. Rev. B **97**, 085154 (2018).
[28] L. Ding, M. Lee, E. S. Choi, J. Zhang, Y. Wu, R. Sinclair, B. C. Chakoumakos, Y. S. Chai, H. D. Zhou, and H. B. Cao, Large

spin-driven dielectric response and magnetoelectric coupling in the buckled honeycomb $Fe_4Nb_2O_9$, Phys. Rev. Mater. **4**, 084403 (2020).

[29] J. Zhang, N. Su, X. R Mi, M. C Pi, H. D Zhou, J. G. Cheng, and Y. S. Chai, Probing magnetic symmetry in antiferromagnetic $Fe_4Nb_2O_9$ single crystals by linear magnetoelectric tensor, Phys. Rev. B **103**, L140401 (2021).

[30] B. H. Toby, EXPGUI, a graphical user interface for GSAS, J. Appl. Cryst. **34**, 210 (2001).

[31] K. Momma and F. Izumi, VESTA 3 for three-dimensional visualization of crystal, volumetric and morphology data, J. Appl. Crystallogr. **44**, 1272 (2011).

[32] L. Ding, M. Lee. T. Hong, Z. L. Dun, R. Sinclair, S. X. Chi, H. K. Agrawal, E. S. Choi, B. C. Chakoumakos, H. D. Zhou, and H. B. Cao, Noncollinear magnetic structure and magnetoelectric coupling in buckled honeycomb $Co_4Nb_2O_9$: A single-crystal neutron diffraction study, Phys. Rev. B **102**, 174443 (2020).

[33] Y. K. Chen, X. Luo, X. X. Ma, C. Xu, B. J. Kang, W. L. Lu, J. C. Zhang, and S. X. Cao, Zero-field ferroelectric state and magnetoelectric coupling in antiferromagnetic $Fe_4Nb_2O_9$ single crystal, Ceram. Int. **47**, 9055 (2021).

[34] X. Li, M. F. Liu, Y. Wang, L. M. Tian, R. Shi, Q. Y. Pan, J. J. Han, B. Xie, X. Z. Wang, S. Z. Li, L. Lin, Z. B. Yan, and J.-M. Liu, Magnetoelectric mutual-control in collinear antiferromagnetic $NdCrTiO_5$, Appl. Phys. Lett. **113**, 122903 (2018).

[35] J. H. Min, S. H. Zheng, J. W. Gong, X. Y. Chen, F. Liu, Y. L. Xie, Y. J. Zhang, Z. Ma, M. F. Liu, X. Z. Wang, H. Li, and J. M Liu, Magnetoelectric effect in garnet $Mn_3Al_2Ge_3O_{12}$, Inorg. Chem. **61**, 86 (2022).

[36] H. Katsura, N. Nagaosa, and A. V. Balatsky, Spin Current and Magnetoelectric Effect in Noncollinear Magnets, Phys. Rev. Lett. **95**, 057205 (2005).

[37] I. A. Sergienko, C. Şen, and E. Dagotto, Ferroelectricity in the Magnetic *E*-Phase of Orthorhombic Perovskites, Phys. Rev. Lett. **97**, 227204 (2006).

[38] T. Arima, Ferroelectricity induced by proper-screw type magnetic order, J. Phys. Soc. Jpn. **76**, 073702 (2007).

[39] M. Matsumoto and M. Koga, Symmetry analysis of magnetoelectric effects in honeycomb antiferromagnet $Co_4Nb_2O_9$, J. Phys. Soc. Jpn. **88**, 094704 (2019).

[40] S.-W. Cheong, Trompe L'oeil ferromagnetism, npj Quant. Mater. **5**, 37 (2020).

[41] S. V. Gallego, J. Etxebarria, L. Elcoro, E. S. Tasci, and J. M. Perez-Mato, Automatic calculation of symmetry-adapted tensors in magnetic and non-magnetic materials: A new tool of the Bilbao Crystallographic Server, Acta Crystallogr. A **75**, 438 (2019).